Oxide Particle Growth During Friction Stir Welding of Fine Grain MA956 Oxide Dispersion-Strengthened Steel

BRAD W. BAKER, KEITH E. KNIPLING, and LUKE N. BREWER

Friction stir welding of an aluminum-containing oxide dispersion-strengthened steel causes significant oxide particle growth visible at both the nano- and microscales. Quantitative stereology of scanning electron images, small-angle X-ray scattering, energy-dispersive X-ray spectroscopy, and atom-probe tomography is used to quantify the degree of particle coarsening as a function of welding parameters. Results show the dispersed oxides are significantly coarsened in the stir zone due to a proposed combination of agglomeration, Ostwald ripening, and phase transformation within the Al_2O_3-Y_2O_3 system. This oxide particle coarsening effectively removes all strengthening contribution of the original oxide particles, as confirmed by uniaxial tensile tests and microhardness measurements.

I. INTRODUCTION

BECAUSE of their high-temperature strength, radiation damage resistance, creep resistance, and corrosion resistance, oxide dispersion-strengthened (ODS) steels are attractive candidates for use in next-generation power production applications.[1–4] A primary concern, however, is developing effective joining techniques for these materials, since traditional fusion welding causes agglomeration of oxide particles resulting in loss of strength and degraded material performance in oxide-depleted areas.[5–9] Solid-state joining techniques, such as friction stir welding (FSW), have thus been pursued, and several authors have demonstrated success in welding various ODS steels.[10–16] In a previous report,[16] FSW was proven to be an effective joining technique for an MA956 ODS steel, producing consolidated welds over a range of welding parameters although sacrificing a portion of the alloy's high-temperature strength.

ODS steels are typically produced by mechanical alloying elemental or pre-alloyed metallic powders with nanoscale yttria (Y_2O_3) particles, followed by consolidation using hot isostatic pressing or hot extrusion. For alloys containing aluminum (typically 4 to 5 wt pct, such as MA956 and PM2000), the original Y_2O_3 particles react with oxidized aluminum in the metal matrix, producing various Y-Al-O compounds during the powder metallurgy process.[17–22] These particles include yttrium aluminum monoclinic (YAM-$Y_4Al_2O_9$), yttrium aluminum perovskite (YAP-$YAlO_3$), and yttrium aluminum garnet (YAG-$Y_3Al_5O_{12}$), which form at progressively higher temperatures and aluminum concentrations.[17] Once formed, these stable equilibrium phases are resistant to further change.[18,19,21,22] Because of the known significance of aluminum in corrosion prevention of ODS alloys in a wide variety of environments including air,[20] super-critical water (SCW),[23] molten lead,[24] and lead bismuth eutectic (LBE),[25] the research presented here focuses on aluminum-containing ODS alloys.

Initial research on the evolution of oxide particles in ODS steels produced inconclusive results on the stability of the oxides during heat treatments or joining methods. More recent research has shown that the oxide particles undergo substantial change during these processes,[26,27] although there is no consensus on the mechanism for this change. While several authors have reported on the effects of FSW on the oxides in ODS steels, there is also no general agreement upon the relationship between FSW parameters and oxide particle size and distribution after welding. Using scanning electron microscopy (SEM) and small-angle neutron scattering (SANS), West concluded that the single FSW parameter condition of 400 revolutions per minute (RPM) and 50 mm per minute (MMPM) resulted in the dispersed oxides being slightly coarsened.[28] Similarly, using high-spatial resolution scanning transmission electron microscopy (STEM), Chen concluded that FSW did not appear to create a major change in size or distribution of oxides in PM2000.[29,30] Finally, in related work, Legendre and Mathon used X-ray microprobe and SANS data to qualitatively observe that FSW (600 RPM and 50 MMPM on PM2000) caused oxide particles to grow in vicinity of the stir zone (SZ).[12,31]

BRAD W. BAKER is with United States Naval Academy, 590 Holloway RD, Rickover Hall Rm 323, Annapolis, MD 21402. Contact e-mail: bbaker@usna.edu KEITH E. KNIPLING is with the Materials Science and Technology Division, U.S. Naval Research Laboratory, Code 6355, Washington, DC 20375. LUKE N. BREWER is with the Metallurgical and Materials Engineering Department, University of Alabama, P.O. Box 870202, Tuscaloosa, AL 35487-0202.
Manuscript submitted July 8, 2016.
Article published online January 4, 2017

The aim of the current research is to determine both qualitatively and quantitatively the formation and growth of both Y-Al-O particles and titanium particles in MA956 following FSW over a range of welding conditions that represent both low and high-heat inputs. The size, spatial distribution, and phases of oxides are determined after FSW for each parameter combination. Finally, this research will determine the macro-level effect of particle changes on the strengthening mechanisms of the alloy to help determine suitability of FSW as a joining mechanism for MA956 and other aluminum-containing ODS steels.

II. EXPERIMENTAL PROCEDURE

A. Materials and Processing

The MA956 alloy studied is a high-Cr ferritic ODS steel with the composition shown in Table I, and is identical to the alloy used in a previous study.[16] The chemical compositions in Table I were measured using inductively coupled plasma mass spectrometry and LECO analysis (Anamet Inc.). The MA956 powder precursors were canned and extruded by Special Metals at 1373 K (1100 °C) and subsequently hot-rolled in three passes at 1373 K (1100 °C) over 4 hours with reheating to 1373 K (1100 °C) for 30 minutes before and after each rolling pass. Unlike most production processes of MA956 done by Special Metals, the MA956 in this research was not subjected to any additional heat treatment after hot rolling. Final machining produced a 4-mm (0.157 inch) thick plate.

FSW of MA956 plate was accomplished by MegaStir Technologies using a tool fabricated from an MS 80 grade of polycrystalline cubic boron nitride (PCBN) and a convex scroll shoulder step spiral (CS4) tool design which requires no tool tilt. The tool used had a 25.4-mm diameter shoulder, 1.72-mm pin length, and 6-mm pin diameter. Plunge force was maintained constant at 17.8 kN (4000 lbf). FSW parameters of tool rotation rate in RPM and tool traverse speed in MMPM were varied to produce eight differing weld conditions. Only those conditions that produced fully consolidated defect-free welds[16] are analyzed in this study: (1) 400 RPM to 100 MMPM (the lowest heat input condition), (2) 300 RPM to 50 MMPM (moderate heat input condition), and (3) 500 RPM to 25 MMPM (the highest heat input condition). A full analysis of heat input during FSW of MA956 and its effect on weld consolidation, grain growth, and resultant material properties is presented separately.[32]

B. Microscopy Techniques

Because of the size of the oxide particles present in MA956 and other ODS alloys, many studies have focused on nanoscale techniques including TEM, SANS, and APT, while neglecting microscale-level effects. Due to the hypothesized coarsening effects of FSW on ODS materials, the present research utilizes both nanoscale (<100 nm, typical of oxide particles in the as-prepared MA956) and microscale (>100 nm) analytical techniques. This denotation is not intended to classify MA956 as a nanostructured ferritic alloy (NFA) as that term is typically reserved for more fine particle-sized alloys such as MA957.[15]

Samples of the FSW MA956 plate were sectioned and analyzed by SEM, EDS, STEM, small-angle X-ray scattering (SAXS), and APT. Transverse cross-sections of each welding condition were prepared by standard metallographic techniques, using SiC papers, aluminum oxide polishing solutions, and 0.05 mm colloidal silica solution. The sections were then electropolished at 20 V using an electrolyte containing 10 pct perchloric acid in ethanol maintained at 250 K (−23 °C).

The microstructures were examined with a Zeiss Neon 40 field emission scanning electron microscope (SEM), operating at 20 keV. Oxide particle growth was measured by quantitative stereology of $67 \times 67\ \mu m^2$ representative sections from the SZ for each FSW condition. Area selection was based on ensuring a sufficient number of particles for statistically accurate counting. The area size selected resulted in a minimum of 647 particles and a maximum of 1972 particles in any given measured area. SEM images from the SZ containing visible oxide particles were analyzed using two different digital stereology software packages: (1) ImageJ, a public domain image processing solution developed by the National Institute of Health and previously used in a variety of microscopy techniques,[33] and (2) a MATLAB code designed by Woertz specifically for measuring particle distribution and homogeneity in FSW of two-phase alloys containing non-deformable particles in a soft matrix.[34] These are comparable to other stereology approaches that have been used on similar ODS alloys.[26] Results from both packages were similar, hence results only from ImageJ are included in this report. Full analysis is available elsewhere.[35]

STEM images were obtained using the same Zeiss Neon 40 field emission SEM at 30 keV, a 30 μm objective aperture, and an approximate probe current of 330 pA on thin-foil samples prepared by twin jet electropolishing of 3 mm disks thinned to less than 100 μm. Electropolishing was accomplished using 10 pct

Table I. Chemical Compositions of MA956 in Weight Percent (Atomic Percent)

C	Cr	Al	Ti	Y₂O₃	Mo	Mn	Ni	S	Si	P	Fe
0.023 (0.10)	19.9 (20.1)	4.75 (9.24)	0.39 (0.43)	0.51 (0.12)	0.02 (0.01)	0.09 (0.09)	0.04 (0.04)	0.008 (0.01)	0.08 (0.15)	0.006 (0.01)	bal. (69.7)

perchloric acid in an ethanol solution maintained at a temperature below 233 K (−40 °C) and 20 V_{DC}. Although high-resolution imaging techniques such as STEM and TEM are required to view nanoscale features, the sample preparation techniques for these methods often cause larger particles to fall out during preparation, as acknowledged in other studies,[12,31] and thus STEM or TEM alone are not adequate to evaluate the broad particle distributions encountered in this research. The use of multiple techniques is considered to be one of the primary advantages of this approach.

C. *Small-Angle X-Ray Scattering Techniques*

Specimens for SAXS were sectioned perpendicular to the weld direction so as to include cross-sections of the base and weld material for both the advancing side (AS) and retreating side (RS) of the weld. The specimens were then metallographically thinned and mechanically polished on both sides to a final thickness of approximately 50 μm using a South Bay Technology TEM lapping fixture. Polishing was performed by sequentially grinding using SiC papers followed by a 6 and 1 μm diamond slurry polish on a nylon cloth, and a final polish using 0.05 μm colloidal silica on a neoprene cloth. SAXS analyses were conducted at the Advanced Photon Source at Argonne National Laboratory (ANL) using the USAXS beamline (15-ID). A more detailed description of the SAXS setup is provided elsewhere.[35]

D. *Energy-Dispersive X-Ray Spectroscopy Techniques*

EDS data were collected at 12 keV with an Apollo 10 EDAX Silicon Drift Detector (SDD) for both individual particles, map areas, and line scans, and the data were analyzed using EDAX Genesis software. All EDS maps were taken from representative areas of either the base metal (BM) or SZ areas and were 23 μm by 17 μm rectangular sections. All EDS point, map, and line spectra were counted for 180 live seconds. This resulted in typical peaks of 10,000 counts or more for elements of interest. Lower beam voltages of 10 and 5 keV were attempted but did not offer improved spatial resolution (5 keV resulted in an insufficient count rate). For this reason, a beam voltage of 12 keV was established and used throughout this research for EDS analysis.

E. *Atom-Probe Tomography Techniques*

The APT specimens were prepared using standard lift-out and focused ion beam (FIB) milling procedures[36] on metallographically polished weld cross-sections using an FEI Nova 600 NanoLab DualBeam SEM/FIB. APT analysis was accomplished in a Cameca LEAP 4000X Si using a 40 K (−233 °C) base temperature, 60 pJ nominal laser pulse energy, a pulse repetition rate of 200 kHz, and a detection rate of six ions per 1000 pulses (0.6 pct). Post-analysis data reconstruction and evaluation were performed with Cameca's IVAS 3.6.12 analysis software. Oxides were isolated and studied quantitatively using the proximity histogram (or proxigram) technique.[37,38]

III. RESULTS

A. *Base Metal Microstructure*

Figure 1 displays the microstructure of the base metal of MA956, prior to FSW. Light and dark micron-scale particles are observed in the scanning electron micrograph, Figure 1(a). The few light particles are Al_2O_3, with negligible amounts of yttrium or other elements, as confirmed by EDS (Figure 1(c)). The dark particles are TiCN (Figure 1(d)). The nanoscale Y-Al-O particles are not visible at this scale, although EDS analysis of the base matrix (Figure 1(e)) exhibits the presence of yttrium as well as the major contributors Fe, Cr, and Al. STEM imaging of BM MA956 (Figure 1(b)) shows a fine grain size, nanoscale Y-Al-O particle distribution, and large dislocation density in the BM due to the hot-rolling fabrication prior to FSW.

An atom-probe reconstruction of the base metal microstructure is presented in Figure 2. The APT analysis contains hundreds of nanoscale Y-Al-O particles and also intersected a grain boundary, as evidenced by the Nb and Ti segregation to the interface. The Y-Al-O oxides are somewhat non-uniformly distributed, with one grain containing a large volume fraction of dispersoids, while an adjacent grain contains significantly fewer particles. The nanoscale Y-Al-O particles appear to be bimodally distributed, with small oxides ~8 nm in diameter and larger oxides that are ~20 to 30 nm in diameter. Compositions of these particles are given in the accompanying proxigrams, which display average solute concentration profiles in the α-Fe matrix and Y-Al-O with respect to a 5 at pct Y isoconcentration surface delineating the two phases in the reconstructions. Both classes of oxides have a Y:Al ratio near unity, and are thus identified as $YAlO_3$ (YAP). None of the larger Al_2O_3, or TiCN particles, apparent in Figure 1, were intercepted by the APT analysis.

The bimodal distribution of base metal particle sizes is better quantified by the data in Figure 3, which presents particle size distributions, as measured by SAXS, for MA956 before and after FSW. Two distinct peaks are visible in the BM nanoscale Y-Al-O particle size distribution, corresponding to particle diameters of 6.4 and 17.9 nm.

B. *Stir Zone Microstructure*

In sharp contrast to the BM, the SZ sections of each FSW parameter combination contain a uniform distribution of microscale Y-Al-O particles and a similar size distribution of TiCN particles to that of the BM. Figure 3 also shows the SAXS analysis of the SZ for each of the three welding conditions studied. After FSW, there is a one to two order of magnitude increase in particle size with a corresponding broadening in the volume distribution. Furthermore, the smallest particles (< 10 nm), most prevalent in the BM, are completely eliminated during FSW.

This particle coarsening is observed directly in Figure 4, which displays SEM images of the SZ of each welding condition investigated. FSW causes the microscale Y-Al-O particles (lighter contrast) within the SZ to
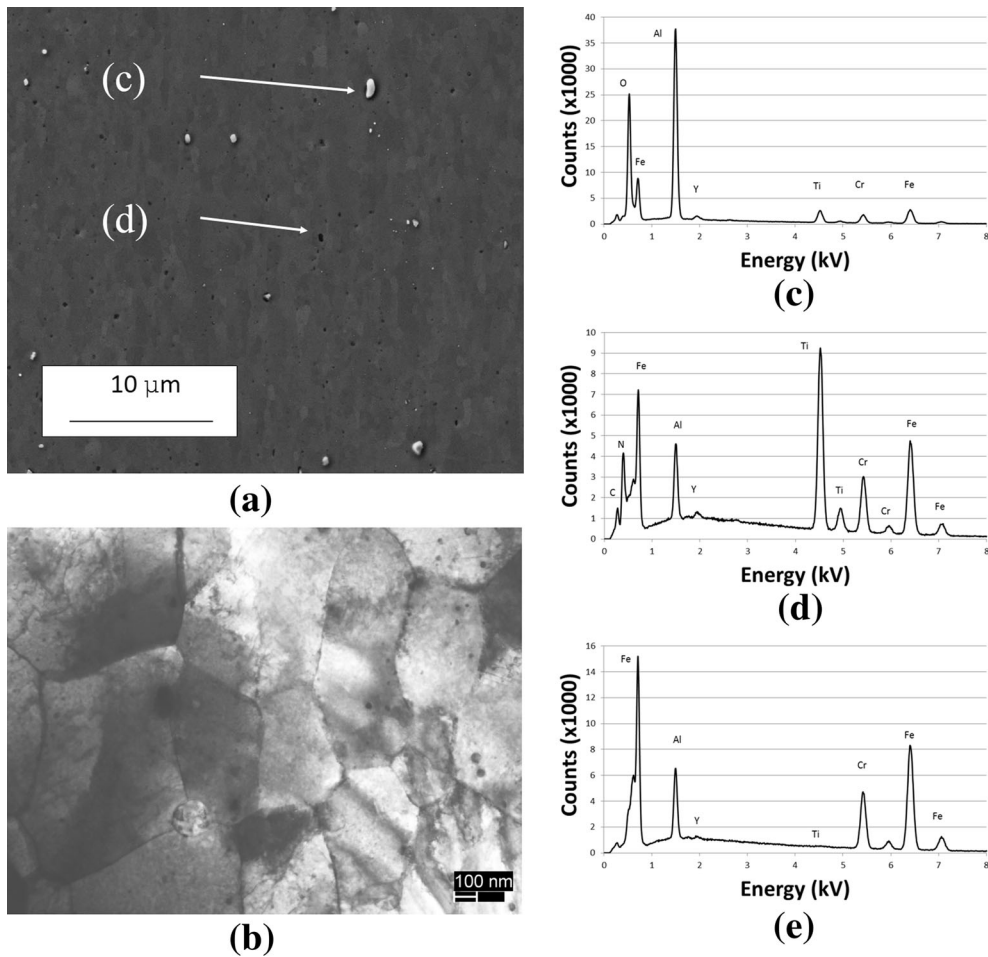
Fig. 1—(a) Scanning electron microscopy image and (b) scanning transmission electron image of base metal MA956 with energy-dispersive X-ray spectroscopy spectra showing (c) Al-O particles (white), (d) TiCN particles (dark) uniformly distributed in the base metal, and (e) the base metal spectrum consisting of primarily Fe, Cr, and Al.
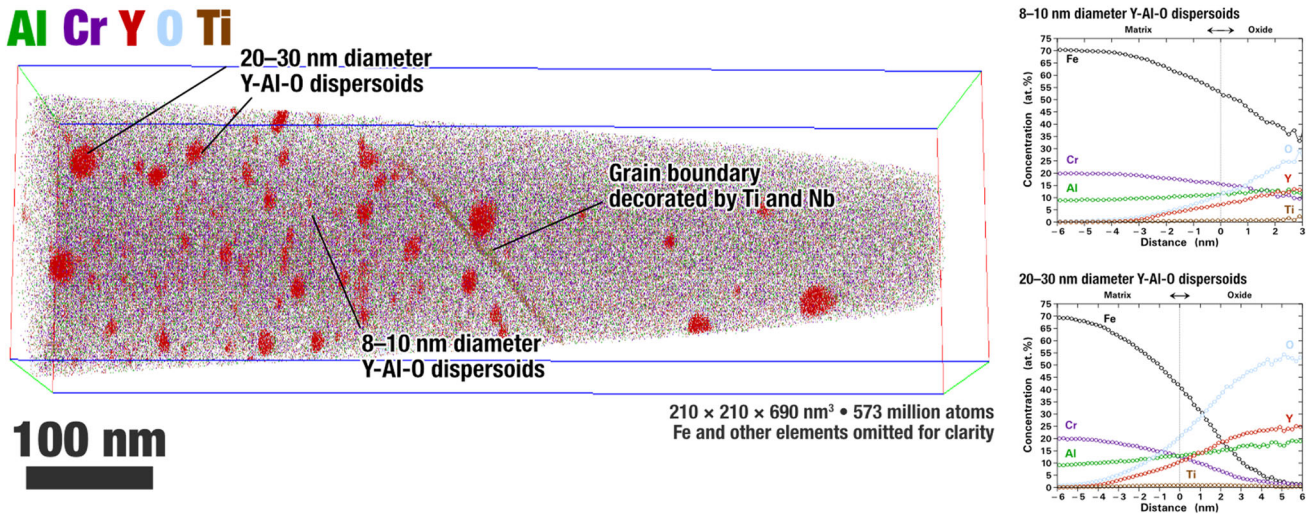

Fig. 2—Atom-probe tomography of base metal MA956 showing a non-uniform distribution of Y-Al-O particles in the Fe–Cr-Al matrix. The accompanying proxigrams display the compositions of the Y-Al-O particles and the surrounding α-Fe matrix.
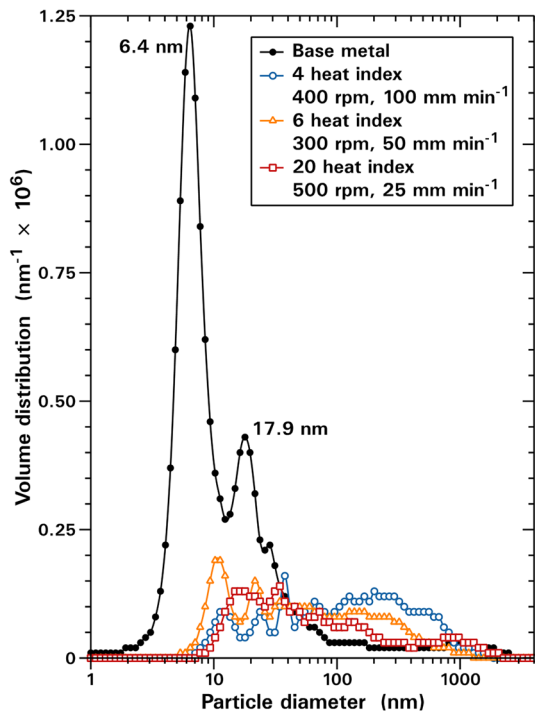
Fig. 3—Small-angle X-ray scattering data indicating the oxide particle sizes in the BM and the SZ after friction stir welding.

increase in average diameter from 226 nm (low-heat input conditions) to 410 nm (high-heat input condition). Grain and oxide particle coarsening results are summarized in Table II. Despite this significant coarsening, the oxides remain homogeneously distributed within the SZ and are not preferentially oriented on grain boundaries. This oxide particle coarsening is also accompanied by significant grain growth, which increases continuously with increasing weld heat input.[32] STEM imaging of the SZ for each welding condition (results not shown here but reported elsewhere[39]) also verified this grain growth and also found a significant reduction in dislocation density due to the continuous dynamic recrystallization during FSW. Dynamic recrystallization is well accepted as the mechanism during FSW and is discussed in detail by Humphreys.[40,41] In contrast to the Y-Al-O particles, the TiCN particles (darker contrast) are not significantly altered by FSW, and maintain a similar size and distribution as that observed in the BM.

EDS mapping of the SZ of each the low and high-heat input welding conditions, Figure 5, showed a clear compositional difference indicating Y-Al-O particle coarsening following FSW that increased as the heat input increased. In addition to the coarsening of Y-Al-O particles, Figures 4 and 5 show a negligible change in titanium particle distribution following FSW for each parameter combination.

C. Oxide Particle Composition

The compositions of the Y-Al-O particles following FSW were determined by quantitative EDS line scans

across oxide particle for the low and high-heat input welding condition, and by APT for the low-heat input condition. YAM, YAP, and YAG are all line compounds on the Al_2O_3-Y_2O_3 phase diagram so the transition between each phase is readily identifiable.[42] For the low-heat input welding condition, 400 RPM to 100 MMPM, a total of 10 particles in the SZ were analyzed by EDS (Figure 6). Of these 10 particles, 7 were determined to by YAG and the remaining 3 (all of which corresponded to larger particles) could not be conclusively be determined to be YAM, YAP, or YAG. For the high-heat input welding condition, 500 RPM to 25 MMPM, 10 particles in the SZ were analyzed by EDS (Figure 7) including a range of particle sizes from large particles (longest axis approximately 500 nm or greater) and small particles (longest axis less than 500 nm). Of these 10 particles, 9 were determined to be YAG with the remaining particle determined to be YAM. The line scans show that YAM forms at an aluminum concentration comparable to the overall aluminum content of MA956 (4.75 wt pct or 9.24 at pct, Table II), while YAG requires a significantly higher aluminum concentration than that in the base alloy. The significance of this observation is discussed later.

An APT reconstruction from the SZ of the low-heat input condition is displayed in Figure 8, which intercepted a coarsened Y-Al-O particle near the end of the analysis. The large, ~300 to 400 nm diameter oxide is composed of two interior regions, ~40 nm in diameter, that are Y-, O-, and S-rich and Al-poor (perhaps YAP or YAM), which are surrounded by an outer shell that is significantly richer in Al (closer to YAG). We hypothesize that the interior Al-poor regions were discreet oxides in the original base metal that agglomerated and coarsened during FSW, and that the aluminum-rich outer phase then formed by diffusion of aluminum from the matrix to the agglomerated particles. This aluminum-driven coarsening mechanism has been suggested by other authors.[26,27]

IV. DISCUSSION

A. Base Metal Microstructure

Prior to FSW, BM MA956 contains nanoscale Y-Al-O particles ranging in diameter from 2 to 80 nm. This distribution is similar to other reported research on BM MA956,[18,21,22] although in the present study, the oxides are bimodally distributed, with most particles having an average diameter of 6.4 nm and a larger, less numerous, class of particles of average diameter of 17.9 nm. These nanoscale particles were identified as YAP by EDS and APT, consistent with other reports on MA956[17] and PM2000.[43]

B. Stir Zone Microstructure

Quantification of oxide particle coarsening is summarized in Table II presented in terms of oxide particle density in the analysis area in particles/m^2 (N), average particle diameter (d_{avg}) in nm, inter-particle
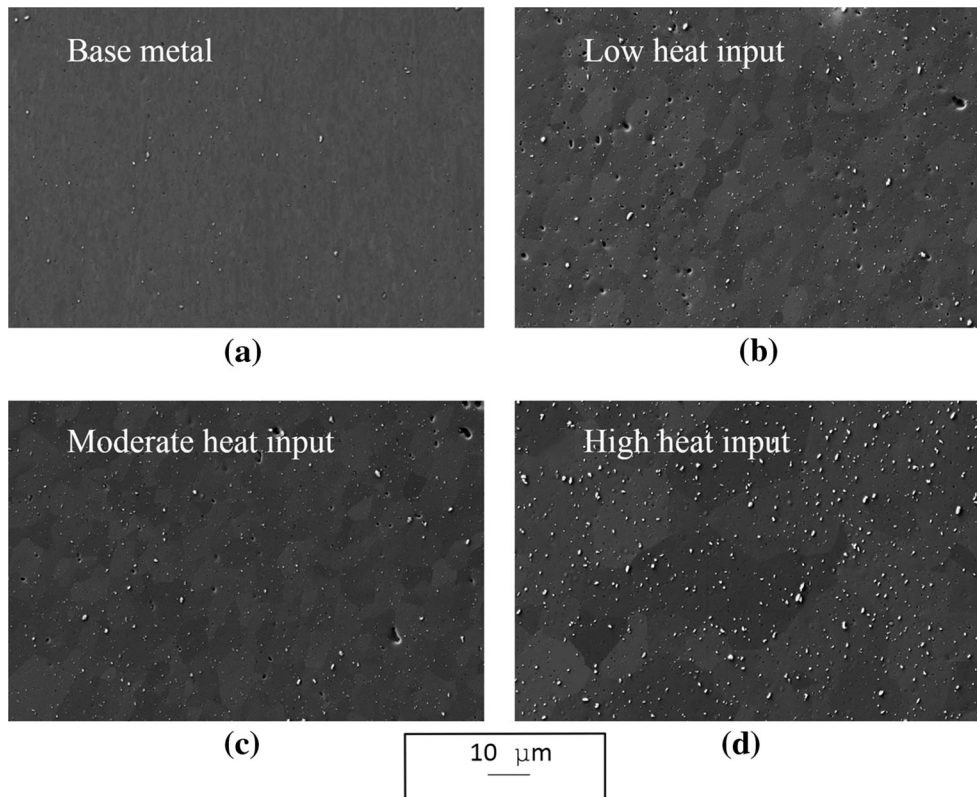
Fig. 4—Scanning electron microscopy image comparison of (*a*) BM, (*b*) 400 RPM/100 MMPM, (*c*) 300 RPM/50 MMPM, and (*d*) 500 RPM/25 MMPM showing oxide particle coarsening following friction stir welding. The 10 micron scale bar applies to all images. Scanning electron microscopy image and (b) scanning transmission electron image of the stir zone for 500 RPM/25 MMPM friction stir welding combination with energy-dispersive X-ray spectroscopy spectra showing (c) coarsened Y-Al-O particles (white) and (d) qualitatively unchanged TiCN particles (dark) uniformly distributed in the base metal.

Table II. Oxide Particle Density (*N*), Average Particle Diameter (*d*$_{avg}$), Inter-particle Spacing (*S*), and Volume Fraction (*f*) for Different FSW Conditions for the Same Sample Area

FSW Parameter Condition (RPM/MMPM)	HI	Average Grain Diameter (μm)	N (Particle/m^2)	d_{avg} (nm)	S (μm)	f (Pct)
400/100	4	6.94	4.02×10^{11}	226	3.23	1.4
300/50	6	4.16	4.13×10^{11}	202	3.19	1.8
500/25	20	12.5	1.44×10^{11}	410	3.41	2.3
BM	—	0.89	—	7.2	—	0.74

Calculations for FSW conditions were accomplished using digital stereology of SEM images and calculations for BM condition was accomplished using APT.

centroid-to-centroid spacing (*S*) in μm, and volume fraction for different values of HI with FSW parameter conditions listed for reference. Additionally, grain coarsening as a function of HI from Reference 32 is included in Table II for reference. The similarity in welding conditions of 400 RPM to 100 MMPM and 300 to 50 RPM causes the data distribution between these two heat input conditions to be indistinguishable, but the difference between the low-heat input conditions and the high-heat input condition of 500 RPM to 25 MMPM is significant as is the disparity between the BM and any of the FSW conditions. Overall, the data from Table II combined with the qualitative results of Figures 4 through 7, *i.e.,* particle population density decreasing and average particle diameter increasing,

clearly demonstrate that Y-Al-O particles are coarsened during FSW and that this coarsening is dependent on welding parameters, specifically that higher heat input conditions cause greater particle coarsening. Despite the significant coarsening during FSW, the oxide particles remain homogenously distributed as evidenced by the near constant inter-particle spacing (S in Table II) and the qualitative analysis shown in Figure 4. This homogenous distribution of coarsened Y-Al-O particles is consistent with the homogeneity results measured by Woertz[34] for distribution of non-deforming particles in a metal matrix following FSW and significantly different than the agglomeration of oxide particles and depletion areas reported during joining using traditional fusion welding techniques.[5–8]
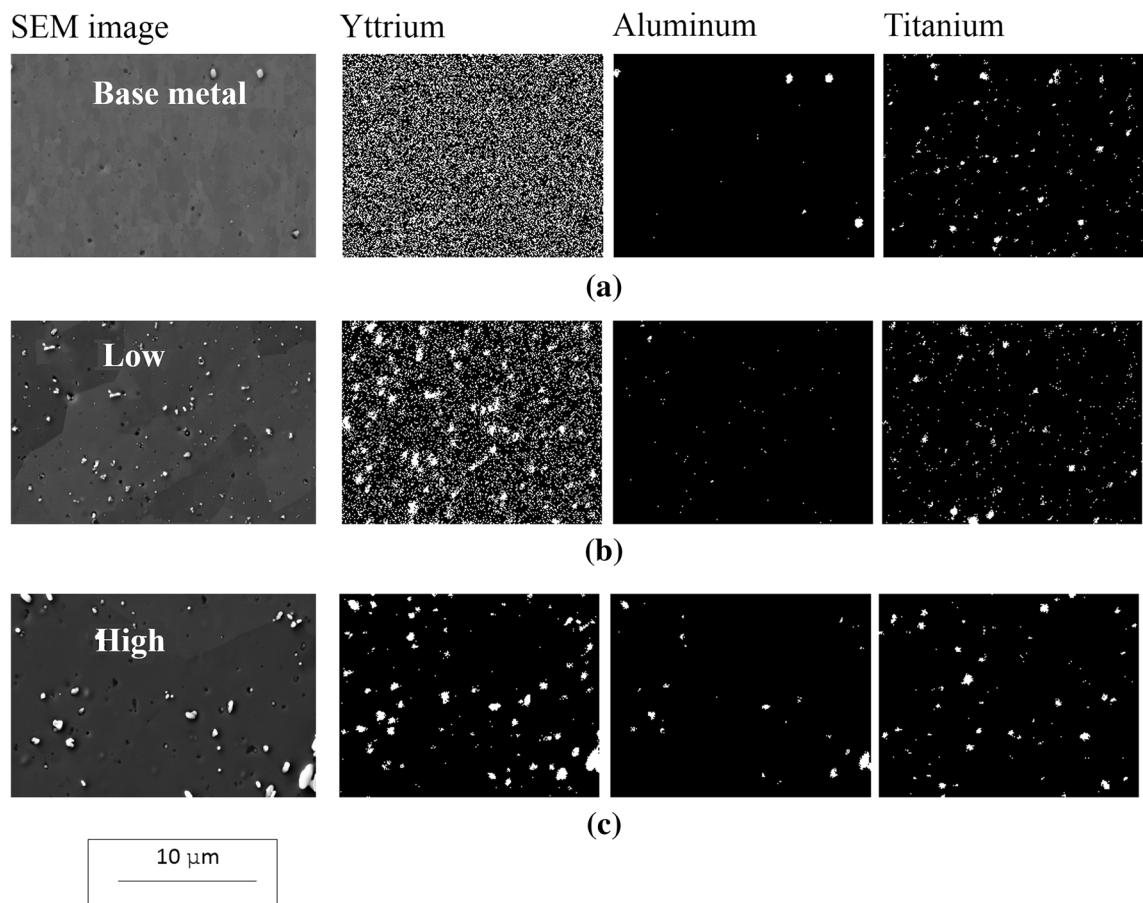
Fig. 5—Scanning electron microscopy imagery and energy-dispersive X-ray spectroscopy spectral maps for yttrium, aluminum, and titanium for (*a*) base metal, (*b*) 400 RPM/100 MMPM (low HI), and (*c*) 500 RPM/25 MMPM (high HI) showing increasing oxide particle coarsening as HI was increased during friction stir welding.

The oxide particle coarsening during FSW presented here is similar to particle coarsening shown by others during extended high-temperature exposure of MA956 at temperatures below its melting temperature.[19,21] Using TEM, Cama[19] observed a three times increase in average particle size (from approximately 15 to 50 nm) during exposure at 1573 K (1300 °C) (88 pct of the melting temperature for MA956) over 1000 hours. Kruk,[21] using electron tomography, observed in excess of a two times increase in particle size (from 3-60 nm to 92-192 nm) during exposure at 1623 K (1350 °C) over 1000 hours. Both of these results show particle increases of roughly the same magnitude seen in this research and are both at temperatures expected during FSW.[44–46] The primary difference is the time scale over which the coarsening occurs. As opposed to the 1000 hours of exposure time of Cama and Kruk, the coarsening during FSW occurs during the short-term welding process. The cause of this difference in coarsening rate is attributed to the proposed coarsening mechanism presented in this paper.

C. *Proposed Coarsening Mechanisms*

Before discussing possible mechanisms behind the oxide particle coarsening seen in this research, a more detailed summary of current literature on oxide particle coarsening in aluminum-containing ODS steels will be presented in order to establish hypotheses for the effects of FSW on the oxide particles. This review includes research on FSW of the ODS steels PM2000 and MA956 which are similar in composition and initial processing.

Using SANS and SEM, West analyzed the change in microstructure of MA956 following FSW with conditions of 400 RPM to 50 MMPM (a comparatively low-heat input condition) and 600 RPM to 13 MMPM (a comparatively high-heat input condition) and concluded that "dispersoids were slightly coarsened during welding" without any quantification of the degree of coarsening or any determination of the phase of the particles either before or after FSW.[28] Using comparisons of grain size and hardness to analyze the change of oxide particle size and distribution, West suggests that oxide particles may have dissolved and re-precipitated during FSW leading to the slight coarsening effect observed.

Using TEM and STEM, Wang researched the change in microstructure and mechanical properties of MA956 following FSW with the comparatively very high-heat input condition of 1000 RPM to 50 MMPM.[11] Although oxide particle phase composition
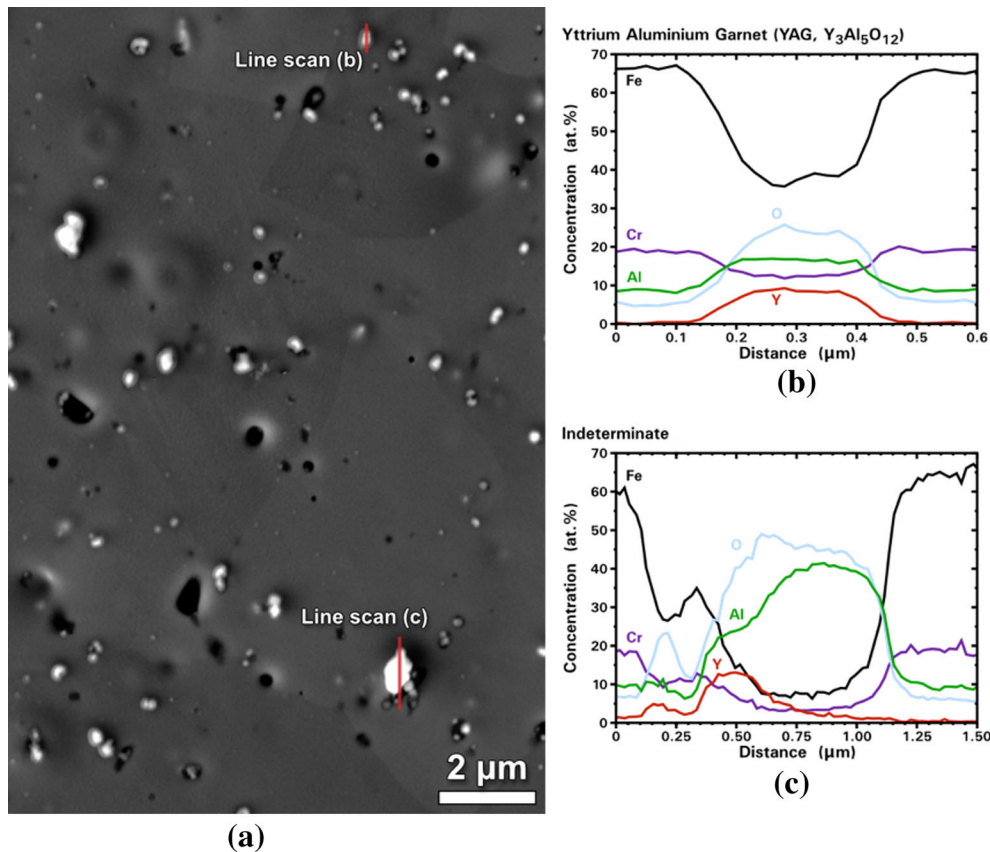
Fig. 6—(a) Scanning electron microscopy image of the stir zone from the low-heat input condition (400 RPM/100 MMPM) showing particles (b) and (c) analyzed by energy-dispersive X-ray spectroscopy.

determination was not attempted, Wang observed dispersoid coarsening and commented "fine dispersoids were noticed to attach to coarse ones, and typical diameter was about 140 nm, which was not observed in the as-received material under TEM."[11] In his conclusions, Wang describes this effect as particle-coalescence-induced coarsening. Although he does not state it as such, Wang's theory for coarsening can also be described as Ostwald ripening.

In related work, Mathon and Legendre analyzed the effects of FSW on the microstructure of PM2000 using SANS and concluded that oxide particles "grow larger as one approaches the SZ. In the nugget of the weld joint, the size of the particles is too large to allow quantifying their size and volume fraction."[12,31] Mathon and Legendre investigated a single high-heat input condition (600 RPM/50 MMPM), comparable to the high-heat input condition used in this research (500 RPM/25 MMPM). The methods used by Mathon and Legendre may be biased, however, to particles of smaller size so a complete analysis of both nanoscale and microscale particles cannot be accomplished. Mathon and Legendre even note this fact stating "only the smallest particles are detected [by SANS] corresponding to a volume fraction of 0.5 pct."[31] Unlike the EDS and APT analysis used in the present research, the SANS techniques employed by Mathon and Legendre cannot

directly identify the different elements or phases within the alloy, and thus, although Mathon concludes that oxide chemical composition is different than in the BM, he concludes the particles in the SZ may be Y-Ti-Al-O without definitive data to support this suggestion. None of the EDS data in this research have shown a change in titanium distribution following FSW that supports the formation of a Y-Ti-Al-O phase. Although neither Mathon nor Legendre propose a mechanism behind the effect of FSW on the oxide particles in PM2000, both of their results suggest a change in the chemical composition of particles following FSW. Recent research on oxide particle coarsening in ODS steels suggests that aluminum plays a prominent role in coarsening due to formation of a new phases.[26,27]

From this literature review, three mechanisms are proposed for the coarsening of Y-Al-O particles observed in this research: (1) particle coarsening due to the dissolution and subsequent re-precipitation of Y-Al-O particles (similar to that presented by West), (2) particle coarsening due to Ostwald ripening (similar to that presented by Wang), and (3) particle coarsening due to phase transformation within the Al_2O_3-Y_2O_3 system similar to that seen during initial alloy consolidation and processing (similar to that presented by Mathon and Legendre). The first coarsening mechanism proposed, dissolution and subsequent re-precipitation of Y-Al-O
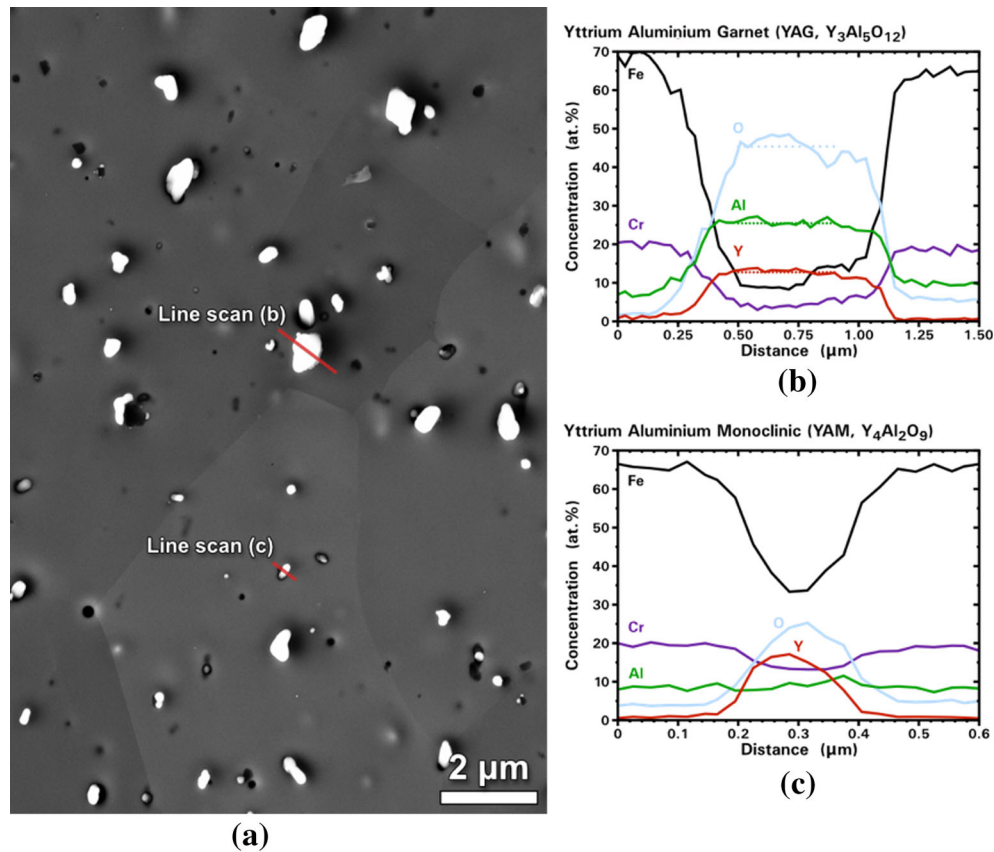
Fig. 7—(a) Scanning electron microscopy image of the stir zone from the high-heat input condition (500 RPM/25 MMPM) showing particles (b) and (c) analyzed by energy-dispersive X-ray spectroscopy.

particles, seems unlikely. While temperature was not monitored during welding of the present alloys, theoretical and other experimental research has shown that FSW raises an alloy to approximately 80 to 90 pct of its absolute melting temperature (equating to a temperature ranging from 1451 K to 1599 K (1178 °C to 1326 °C) for MA956).[44–48] This temperature is insufficient to cause dissolution of any phase in the Al_2O_3-Y_2O_3 system,[42] and other experimental work has shown the ability to melt the base metal alloy while preserving the oxides intact for analysis.[49] Additionally, the enthalpies of formation for YAG (−7197 kJ/mol), YAM (−5545 kJ/mol) and YAP (−1827 kJ/mol)[50] are sufficiently low to suggest that dissolution of any of these phases is unlikely even during FSW. Research on the phase stability of YAG, YAM, and YAP also suggests these phases would not undergo dissolution at the temperatures typically seen during FSW.[51]

The second proposed mechanism, Ostwald ripening, dictates that larger particles grow at the expense of smaller particles in a constant volume fraction process and is discussed in detail by Voorhees.[52] Taken on their own, the SAXS results in this research (Figure 3), or any method that does not include an analysis of phase, suggest Ostwald ripening as a mechanism for oxide particle coarsening. These methods show a reduction in population of smaller particles and an increase in population of larger particles and inherently assume a

constant volume fraction process of the second phase, i.e., the Y-Al-O particles.

The volume fraction (f) of a precipitate is directly related to the diameter of the precipitate (d) and the inter-particle spacing (S) of the precipitates (Eq. [1]).[53]

$$f = \frac{1/6\pi d_{avg}^3}{S^3} \qquad [1]$$

For the BM condition, volume fraction can be calculated directly from the chemical analysis as shown in Table I. The quantitative stereology used in this research measures particle diameter (d_{avg}), inter-particle spacing (S), and particle area fraction which was converted to volume fraction (f) based on a homogenous distribution of particles. From Eq. [1] and the consistency of S over different welding conditions, particle growth does not follow a constant volume fraction process.

The third proposed coarsening mechanism, particle coarsening due to phase transformation within the Al_2O_3-Y_2O_3 system, by itself does not explain the specific reasoning behind the coarsening and also does not fully address whether the YAG particles are formed from existing YAM or YAP particles or whether they originate from the original Y_2O_3 and Al_2O_3 reactants; however, the EDS data and APT data from this research conclusively demonstrate that a new Y-Al-O phase (i.e.,
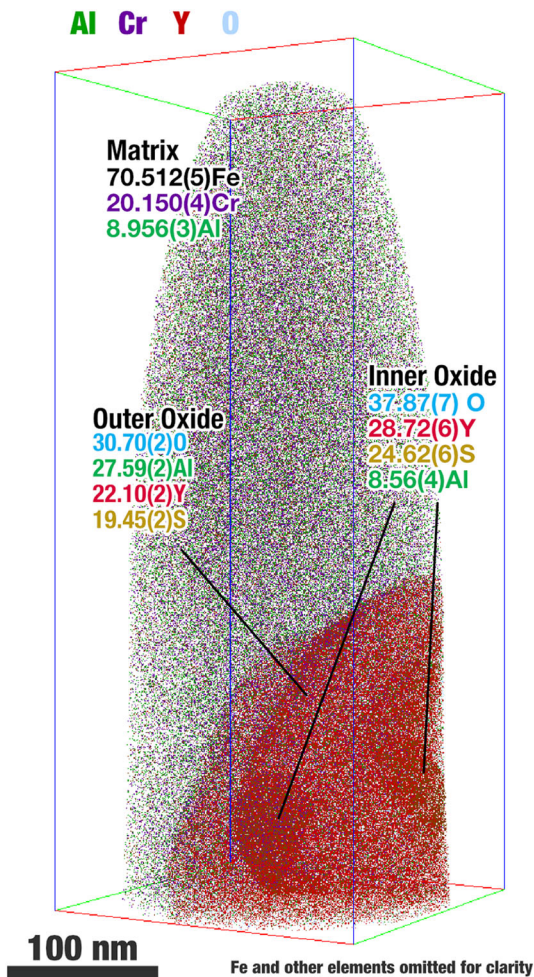
Fig. 8—Atom-probe tomography reconstruction of the low-heat input conditions showing significant particle coarsening from the base metal. The ~300 to 400 nm diameter particle is composed of two ~40 nm diameter interior regions that are yttrium-, oxygen-, and sulfur-rich and aluminum-poor, that is surrounded by an aluminum-rich outer phase. The compositions (in at pct) of both of these oxide phases and the surrounding matrix are indicated in the figure.

YAG) has formed that did not previously exist in the BM. It is proposed that during the thermal and plastic deformation cycles of FSW, aluminum and oxygen in the metal matrix diffuse to form the new YAG phase thus increasing the size of the particle. Moreover, the APT results (Figure 8) suggest that a second aluminum-rich phase forms on the outer edges of existing oxides creating a new larger and non-homogenous particle. Because of these effects, the coarsening of oxides in MA956 is concluded to be from a combination of agglomeration, Ostwald ripening, and phase transformations within the Al_2O_3-Y_2O_3 system. The phase transformations were observed by Hsiung on the same MA956 as used in this research, although the manufacturing treatments used did not expose the MA956 to temperatures in the range of YAG formation (approximately 1673 K (1400 °C)); however, the same MA956, now friction stir-welded, can be expected to have

reached temperatures up to 90 pct of the melting temperature and thus very close to the range of YAG formation.

D. Titanium Particle Effects

Titanium particles (generally reported to be TiCN) reported in several ODS alloys are of less importance in aluminum-containing ODS alloys since Y-Al-O particles preferentially form over Y-Ti-O particles.[26,27,54,55] It is notable that in several aluminum-free ODS alloys, such as MA957 and 12/14YWT, Y-Ti-O particles form that have different formation mechanisms and potentially a different evolution during FSW.[56–58] The dispersed titanium particles in MA956 appear to be unaffected by FSW up to the heat input used here (Figure 7). Similar research on MA957 (an ODS alloy without aluminum) with a singular FSW condition has shown that FSW had relatively little effect on the number density and size distribution of Y-Ti-O particles.[15,56] Whether Y-Ti-O particles are stable during all FSW conditions is unknown, but the difference in response of Y-Al-O ODS alloys and Y-Ti-O ODS alloys may give additional options when considering various alloys for design applications.

E. Impact on Material Properties

The oxide particle coarsening and grain growth following FSW have a significant effect on the overall yield strength of the welded joint and essentially removes all strengthening contribution of the dispersed oxides. Full analysis of tensile behavior of friction stir-welded MA956 is available in related research[39] and closely matches other literature sources that determine that strengthening contribution of the dispersed oxides in MA956.[11,49,59] The results of this related research are clearly visible on an experimentally determined Hall–Petch plot of MA956 (Figure 9) which shows the grain size dependence of yield strength as well as the effect oxide particle coarsening from the BM condition. The data for Figure 9 are presented in detail in Reference 39 and are provided here to show the material impact of grain and oxide particle coarsening.

V. CONCLUSIONS

This paper has provided a systematic analysis of oxide particle coarsening after FSW of the ODS steel MA956 using a variety of techniques. Oxide particle transformation begins during phase transformation manufacturing of the base alloy and continues during FSW. The degree of coarsening has a significant effect on the strengthening contribution of the particles. The following conclusions were drawn:

1. FSW causes significant coarsening of existing Y-Al-O particles within the SZ of MA956. The coarsening is evident both at the nanoscale by a reduction in nano- sized particles and at the microscale by an observed increased in micro-sized particles. This
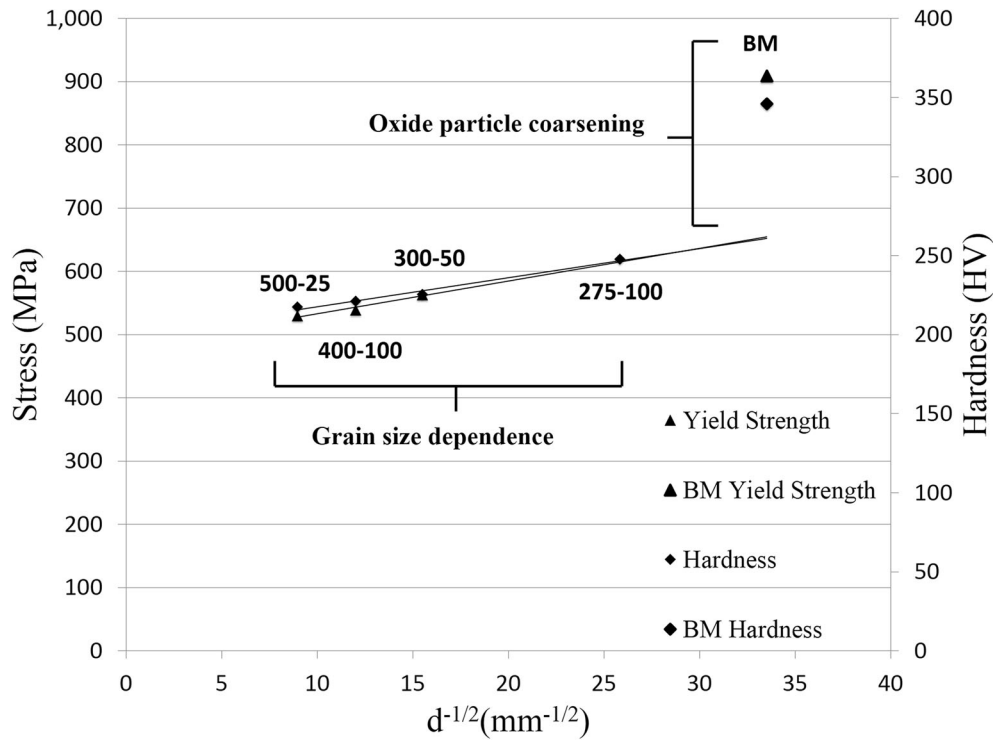
Fig. 9—Comprehensive experimentally determined Hall–Petch plot of MA956 using data from Refs. 15 and 39 showing grain size dependence of yield strength and the effect of oxide particle coarsening from the base metal (BM) condition (open markers). Data points (solid markers) are from the stir zones of different friction stir welding parameter conditions in RPM-MMPM.

oxide particle coarsening is attributed to a combination of agglomeration, Ostwald ripening, and a continuance of phase transformations within the Al_2O_3-Y_2O_3 system. The coarsening produces non-homogenous particles that have inner and outer oxides layers that differ primarily in aluminum concentration suggesting that aluminum is a key factor in coarsening. Unlike traditional fusion welding techniques, oxides are homogenously coarsened within the weld nugget.

2. The degree of oxide particle coarsening is a function of welding conditions. FSW conditions with high-thermal input can cause up to a two times increase in average particle size as compared to low-heat input conditions. Increased heat input did not change the inter-particle spacing of particles suggesting that a constant volume fraction process assumption is not appropriate.

3. Titanium particles in ODS alloys containing aluminum are unaffected by FSW and qualitatively do not change in size nor form Y-Ti-O particles due to the preferential formation of Y-Al-O particles.

ACKNOWLEDGMENTS

REFERENCES

1. E.E. Bloom: *J. Nucl. Mater.*, 1998, vol. 258, pp. 7–17.
2. S. Ukai, T. Nishida, T. Okuda, and T. Yoshitake: *J. Nucl. Sci. Technol.*, 1998, vol. 35, pp. 294–300.
3. M.S. El-Genk and J.M. Tournier: *J. Nucl. Mater.*, 2005, vol. 340, pp. 93–112.
4. I. Charit, K.L. Murty, and C.C. Koch: *Advances in Materials Technology for Fossil Power Plants: Proceedings from the Fifth International Conference 2007*, ASM International, Materials Park, OH, 2008, pp. 281–92.
5. M.G. McKimpson and D. Odonnell: *JOM*, 1994, vol. 46, pp. 49–51.
6. R. Lindau, M. Klimenkov, U. Jaentsch, A. Moeslang, and L. Commin: *J. Nucl. Mater.*, 2011, vol. 416, pp. 22–29.
7. H.J.K. Lemmen, K.J. Sudmeijer, I.M. Richardson, and S. van der Zwaag: *J. Mater. Sci.*, 2007, vol. 42, pp. 5286–95.
8. P. Miao, G.R. Odette, J. Gould, J. Bernath, R. Miller, M. Alinger, and C. Zanis: *J. Nucl. Mater.*, 2007, vol. 367, pp. 1197–202.
9. B.W. Baker and L.N. Brewer: *JOM*, 2014, vol. 66, pp. 2442–57.
10. S. Noh, R. Kasada, A. Kimura, S.H.C. Park, and S. Hirano: *J. Nucl. Mater.*, 2011, vol. 417, pp. 245–48.
11. J. Wang, W. Yuan, R.S. Mishra, and I. Charit: *J. Nucl. Mater.*, 2013, vol. 432, pp. 274–80.
12. F. Legendre, S. Poissonnet, P. Bonnaillie, L. Boulanger, and L. Forest: *J. Nucl. Mater.*, 2009, vols. 386–88, pp. 537–39.
13. W. Han, S. Ukai, F. Wan, Y. Sato, B. Leng, H. Numata, N. Oono, S. Hayashi, Q. Tang, and Y. Sugino: *Mater. Trans.*, 2012, vol. 53, pp. 390–94.

14. B.K. Jasthi, S.M. Howard, W.J. Arbegast, G.J. Grant, S. Koduri, and D.R. Herling: in *Friction Stir Welding Processing III*, TMS, San Francisco, CA, 2005, pp. 75–79.
15. A. Etienne, N.J. Cunningham, Y. Wu, and G.R. Odette: *Mater. Sci. Technol.*, 2011, vol. 27, pp. 724–28.
16. B.W. Baker, L.N. Brewer, E.S.K. Menon, T.R. McNelley, B. El-dasher, S. Torres, J.C. Farmer, M.W. Mahoney, and S. Sanderson, in *Friction Stir Welding and Processing VII*, R.S. Mishra, M.W. Mahoney, S. Yutaka, Y. Hovanski, and R. Verma, eds., Wiley, New York, 2013.
17. L.L. Hsiung, M.J. Fluss, S.J. Tumey, B.W. Choi, Y. Serruys, F. Willaime, and A. Kimura: *Phys. Rev. B*, 2010, vol. 82, p. 184103.
18. C.H. Zhang, A. Kimura, R. Kasada, J. Jang, H. Kishimoto, and Y.T. Yang: *J. Nucl. Mater.*, 2011, vol. 417, pp. 221–24.
19. H. Cama and T.A. Hughes: in *Conference of the Electron-Microscopy-and-Analysis-Group of the Institute-of-Physics: Electron Microscopy and Analysis 1993 (EMAG93)*, Liverpool, England, 1993, pp. 361–64.
20. H. Cama and T.A. Hughes: *Scripta Metall. Mater.*, 1995, vol. 32, pp. 1585–88.
21. A. Kruk, B. Dubiel, and A. Czyrska-Filemonowicz: in *Electron Microscopy XIV*, vol. 186, D. Stroz and K. Prusik, eds., Trans Tech Publications, Pfaffikon, 2012.
22. M.F. Hupalo, M. Terada, A.M. Kliauga, and A.F. Padilha: *Materialwiss. Werkstofftech.*, 2003, vol. 34, pp. 505–08.
23. H.S. Cho, A. Kimura, S. Ukai, and M. Fujiwara: *J. Nucl. Mater.*, 2004, vol. 329, pp. 387–91.
24. R.C. Asher, D. Davies, and S.A. Beetham: *Corros. Sci.*, 1977, vol. 17, pp. 545–57.
25. S. Takaya, T. Furukawa, K. Aoto, G. Muller, A. Weisenburger, A. Heinzel, M. Inoue, T. Okuda, F. Abe, S. Ohnuki, T. Fujisawa, and A. Kimura: *J. Nucl. Mater.*, 2009, vol. 386, pp. 507–10.
26. D. Catalini, D. Kaoumi, A.P. Reynolds, and G.J. Grant: *Metall. Mater. Trans. A*, 2015, vol. 46A, pp. 4730–39.
27. C. Capdevila, G. Pimentel, M.M. Aranda, R. Rementeria, K. Dawson, E. Urones-Garrote, G.J. Tatlock, and M.K. Miller: *JOM*, 2015, vol. 67, pp. 2208–15.
28. M. West, B. Jahsthi, P. Hosemann, and V. Sodesetti: in *Friction Stir Welding and Processing VI*, TMS, Warrendale, PA, 2011, pp. 33–40.
29. C.L. Chen, P. Wang, and G.J. Tatlock: *Mater. High Temp.*, 2009, vol. 26, pp. 299–303.
30. C.L. Chen, G.J. Tatlock, and A.R. Jones: *J. Alloys Compd.*, 2010, vol. 504, pp. S460–66.
31. M.H. Mathon, V. Klosek, Y. de Carlan, and L. Forest: *J. Nucl. Mater.*, 2009, vol. 386, pp. 475–78.
32. B. Baker, E.S. Menon, T. McNelley, L. Brewer, B. El-Dasher, J. Farmer, S. Torres, M. Mahoney, and S. Sanderson, *Metall. Trans. E,* 2014, pp. 1–13.
33. T.J. Collins: *Biotechniques*, 2007, vol. 43, pp. S25–30.
34. J. Woertz: PhD Dissertation, Mechanical and Aerospace Engineering Department, Naval Postgraduate School, Monterey, CA, 2013.
35. B.W. Baker: PhD Dissertation, Mechanical and Aerospace Engineering Department, Naval Postgraduate School, Monterey, CA, 2013.
36. K. Thompson, D. Lawrence, D. Larson, J. Olson, T. Kelly, and B. Gorman: *Ultramicroscopy*, 2007, vol. 107, pp. 131–39.
37. O.C. Hellman, J.B. du Rivage, and D.N. Seidman: *Ultramicroscopy*, 2003, vol. 95, pp. 199–205.
38. O.C. Hellman, J.A. Vandenbroucke, J. Rüsing, D. Isheim, and D.N. Seidman: *Microsc. Microanal.*, 2000, vol. 6, pp. 437–44.
39. B.W. Baker, T.R. McNelley, and L.N. Brewer: *Mater. Sci. Eng., A*, 2014, vol. 589, pp. 217–27.
40. F.J. Humphreys: *Acta Mater.*, 1997, vol. 45, pp. 5031–39.
41. F.J. Humphreys: *Acta Mater.*, 1997, vol. 45, pp. 4231–40.
42. J.L. Caslavsky and D. Viechnicki: *Am. Ceram. Soc. Bull.*, 1982, vol. 61, p. 808.
43. Y.Z. Shen, T.T. Zou, S. Zhang, and L.Z. Sheng: *ISIJ Int.*, 2013, vol. 53, pp. 304–10.
44. R.S. Mishra and Z.Y. Ma: *Mater. Sci. Eng., R*, 2005, vol. 50, pp. 1–78.
45. R. Nandan, T. DebRoy, and H.K.D.H. Bhadeshia: *Prog. Mater Sci.*, 2008, vol. 53, pp. 980–1023.
46. R. Nandan, G.G. Roy, T.J. Lienert, and T. DebRoy: *Sci. Technol. Weld. Join.*, 2006, vol. 11, pp. 526–37.
47. M.W. Mahoney, C.G. Rhodes, J.G. Flintoff, R.A. Spurling, and W.H. Bingel: *Metall. Mater. Trans. A*, 1998, vol. 29A, pp. 1955–64.
48. J.W. Qian, J.L. Li, F. Sun, J.T. Xiong, F.S. Zhang, and X. Lin: *Scripta Mater.*, 2013, vol. 68, pp. 175–78.
49. A.Y. Badmos and H. Bhadeshia: *Mater. Sci. Technol.*, 1998, vol. 14, pp. 1221–26.
50. O. Fabrichnaya, H.J. Seifert, R. Weiland, T. Ludwig, F. Aldinger, and A. Navrotsky: *Z. Metall.*, 2001, vol. 92, pp. 1083–97.
51. J.S. Abell, I.R. Harris, B. Cockayne, and B. Lent: *J. Mater. Sci.*, 1974, vol. 9, pp. 527–37.
52. P.W. Voorhees: *J. Stat. Phys.*, 1985, vol. 38, pp. 231–52.
53. M. Meyers and K. Chawla, *Mechanical Behavior of Materials*, 2nd edn, Cambridge University Press, Cambridge, 2009.
54. H. Regle and A. Alamo: *J. Phys. IV*, 1993, vol. 3, pp. 727–30.
55. A. Alamo, H. Regle, G. Pons, and J.L. Bechade: in *Mechanical Alloying*. vol. 88, P.H. Shingu, ed., Trans Tech Publications, Pfaffikon, 1992, pp. 183–90.
56. Y. Wu, E.M. Haney, N.J. Cunningham, and G.R. Odette: *Acta Mater.*, 2012, vol. 60, pp. 3456–68.
57. P. Unifantowicz, R. Schaeublin, C. Hebert, T. Plocinski, G. Lucas, and N. Baluc: *J. Nucl. Mater.*, 2012, vol. 422, pp. 131–36.
58. S.Y. Zhong, J. Ribis, V. Klosek, Y. de Carlan, N. Lochet, V. Ji, and M.H. Mathon: *J. Nucl. Mater.*, 2012, vol. 428, pp. 154–59.
59. A.Y. Badmos, H. Bhadeshia, and D.J.C. MacKay: *Mater. Sci. Technol.*, 1998, vol. 14, pp. 793–809.